Available online at www.sciencedirect.com
ScienceDirect
Journal of Power Sources 171 (2007) 1010–1022
JOURNAL OF POWER SOURCES
www.elsevier.com/locate/jpowsour

Advances in Fe(VI) charge storage Part II. Reversible alkaline super-iron batteries and nonaqueous super-iron batteries

Xingwen Yu [a,*], Stuart Licht [b]

[a] *Department of Chemical and Biological Engineering, The University of British Columbia, 2360 East Mall, Vancouver, BC, Canada V6T 1Z3*
[b] *Department of Chemistry, University of Massachusetts, Boston, MA 02125, USA*

Received 15 June 2007; accepted 15 June 2007
Available online 23 June 2007

Abstract

Reversible thin film Fe(VI/III) cathodic charge/discharge storage in alkaline batteries is presented. Whereas ultra-thin (e.g., 3 nm) Fe(VI/III) films exhibit a high degree of reversibility, thicker films are increasingly passive toward the Fe(VI) charge transfer. An extended conductive matrix facilitates a 100-fold enhancement in charge storage for reversible Fe(VI/III) super-iron thin films. The thicker (100s of nanometers) films deposited on extended conductive matrixes composed of high-surface-area Pt, Ti, and Au can sustain high reversibility, which provides the possibility of using Fe(VI) salts as the cathode materials for rechargeable Fe(VI)/metal hydride batteries. Super-iron cathodes can also be discharged in conjunction with a Li anode in nonaqueous media. Optimization of the nonaqueous primary super-iron/Li batteries is summarized. Fe(VI) cathodes are also reversible in nonaqueous electrolyte systems. The charge/discharge process of super-iron cathodes in nonaqueous media involves both the lithiation/delithiation of the active mass and the reduction/oxidation of the Fe(VI/III), while only the thin film Fe(VI/III) electrodes can sustain high reversibility involving the full theoretical capacity in the nonaqueous batteries.

Keywords: Fe(VI); Super-iron battery; Reversibility; Thin film; Alkaline; Nonaqueous

1. Introduction

Hexavalent iron species (Fe(VI)) have been known for over a century and have long been investigated as the oxidant for water purification [1–3], and as the catalysts in organic synthesis [4,5]. From the late 1990s, Fe(VI) compounds have been investigated as the cathodic charge storage materials for batteries [6–32], as these Fe(VI) salts can sustain facile and energetic cathodic charge transfer. Resources to prepare Fe(VI) salts are plentiful and clean. Iron is the second most abundant metal in the earth's core, and the Fe(VI) reduction product is non-toxic ferric oxide. Fe(VI) salts also exhibit substantially higher cathodic storage capacity than conventional cathodes [6–32].

In addition to primary batteries, society's use of secondary (rechargeable) energy storage is ever growing. While rechargeable lithium and metal hydride anodes have increased the energy capacity of batteries, further advances are limited by the low energy capacity of their cathodes. New higher capacity, environmentally benign and cost effective cathode materials are needed. Recently, research efforts on Fe(VI) electrochemistry are growing [33–36]. Favorable battery cathode characteristics are low solubility, high stability, facile charge transfer, high charge capacity, and an oxidative electrochemical potential. Insoluble cathodes avoid solution phase decomposition, prevent cathode diffusion, chemical reaction with the anode, and self-discharge. Fe(VI) salts are insoluble in a wide variety of nonaqueous solvents [7,9], including electrolytes conducive to studies of Li electrochemistry such as acetonitrile, propylene and ethylene carbonate, γ-butyrolactone, and dimethoxyethane. In nonaqueous media, lithium and Li-ion compatible super-iron cathodes containing either a Li_2FeO_4, K_2FeO_4, $SrFeO_4$ or $BaFeO_4$ cathode have been studied. These Fe(VI) cathodes exhibited high cathodic discharge capacities, respectively, approaching 600, 400, 380 and 310 mAh g^{-1} [9,21]. The nonaqueous discharge of Fe(VI) also incorporates a $3e^-$ Fe(VI) reduction, together with a reaction of Li ion [32].

* Corresponding author. Tel.: +1 604 728 8895; fax: +1 604 822 6003.
E-mail address: xingwenyu@yahoo.com (X. Yu).

0378-7753/$ – see front matter © 2007 Elsevier B.V. All rights reserved.
doi:10.1016/j.jpowsour.2007.06.064

The most recent development in super-iron cathode chemistry is that it is reversible, which has led to the demonstration of rechargeable super-iron batteries. In accord with recent studies [22,24,30,32], the principal limitation to Fe(VI) reversibility has been the passivation of Fe(VI)/Fe(III) redox couple due to resistive buildup of low-conductivity ferric salts. Recently, it has been shown that ultra-thin Fe(VI) layers are reversible cathodes. Consequently they are rechargeable in electrolytes, respectively, conducive to both lithium-ion [32] and metal hydride [24,30] anode batteries. This review paper first focuses on the reversible alkaline super-iron cathodes, then provides a summary of the primary and rechargeable nonaqueous super-iron batteries.

2. Rechargeable alkaline Fe(VI/III) thin film cathodes

While primary charge transfer of super-iron batteries has been demonstrated, reversible charge transfer of Fe(VI) cathode has always been problematic. The poor reversibility of the Fe(VI) cathode is attributed to the conductivity constraints imposed by the ferric oxide product of reduced Fe(VI) [20,24]. However, a sufficient thin film Fe(VI/III) cathode prepared on a conductive matrix (such as Pt or an extended conductive matrix) should facilitate adequate electronic communication to sustain cycled charge storage [24]. In this section this reversibility is demonstrated, using increasingly thick Fe(VI/III) thin films ranging from nanometers to 100s of nanometers in thickness. The thin Fe(VI/III) film half cell charge/discharge behavior was investigated using a three-electrode, sandwiched electrochemical cell with a cation selective membrane (Nafion® 350) to isolate the cathodic and anodic cell compartments (isolate the Fe(VI/III) film electrode with the counter and reference electrode). A saturated calomel electrode (SCE) was used as the reference electrode and a piece of nickel sheet was used as the counter electrode. In full cell studies, the counter electrode and reference electrode were replaced with a metal hydride anode removed from a Powerstream® (Orem Utah, USA) 40 mAh Ni-NiOOH coin cell [24,30]. In both half and full cell studies, 10 M NaOH was used as the electrolyte.

2.1. Reversible Fe(VI/III) ultra-thin film on smooth Pt

In 2004, Licht's group reported that rechargeable ferric films could be generated, as formed by electrodeposition onto conductive substrates from solution phase alkaline Fe(VI) electrolytes

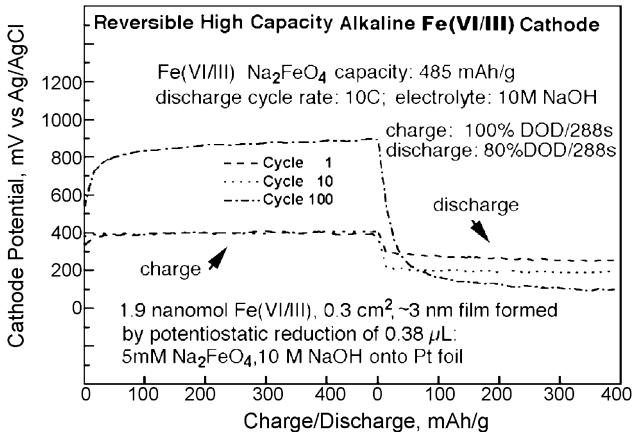

Fig. 1. Reversible charge storage of a Fe(VI) of a 485 mAh g^{-1} capacity Na_2FeO_4 nanofilm. Each galvanostatic storage cycle is 100% DOD charge followed by 80% DOD discharge, at the 10*C* discharge rate [24].

[24]. A thin film, conducive to Fe(VI) charge cycling, was generated on a smooth Pt foil electrode from micro-pipette controlled, microliter volumes of dissolved Fe(VI) in alkaline solution. It was observed that a nanofilm (for example, a 3 nm thickness Fe(VI) film) formed by electrodeposition was highly reversible [24]. This film was rigorous, and when used as a storage cathode, exhibited charging and discharging potentials characteristic of the Fe(VI) redox couple, and extended, substantial reversibility. Fig. 1 presents a three Faraday capacity, reversible Fe(VI/III) cathode. As seen in the figure, a full 80% DOD (depth of discharge) of the 485 mAh g^{-1} capacity Na_2FeO_4 film is readily evident after 100 galvanostatic cycles [24].

2.2. Passivation of thick Fe(VI/III) charge transfer on smooth platinum

As shown in Fig. 1, ultra-thin (3 nm thick) super-iron films can sustain over 100 charge/discharge cycles. However, thicker films were not rechargeable due to the irreversible buildup of passivating (resistive) Fe(III) oxide formed during film reduction, as illustrated in Fig. 2.

3 nm and 19 nm Fe(VI/III) films on Pt are compared in Fig. 3 (left side of Fig. 3 is the expanded results from Fig. 1). As evident, a 3 nm Fe(VI/III) film exhibits reversible behavior throughout 20 galvanostatic charge/discharge cycles, whereas a

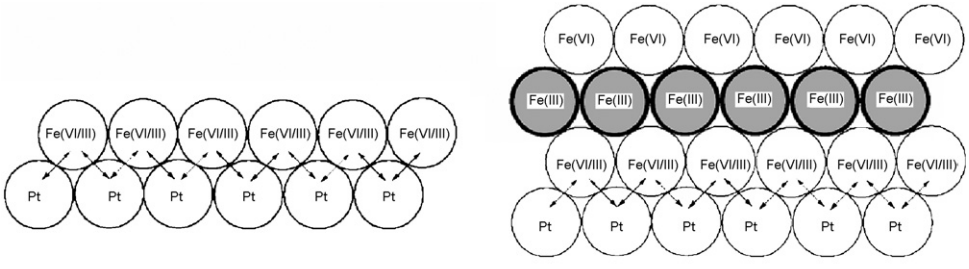

Fig. 2. Representation of facile charge transfer, or passivation, in Fe(VI/III) ferrate films. Left side: reversible Fe(VI/III) charge transfer in a ferrate film without a passivating layer. Right side: the buildup of resistive Fe(III) (depicted by shade), situated between outer Fe(VI) and the cathode current collector, can impede thicker ferrate film charge transfer [30].

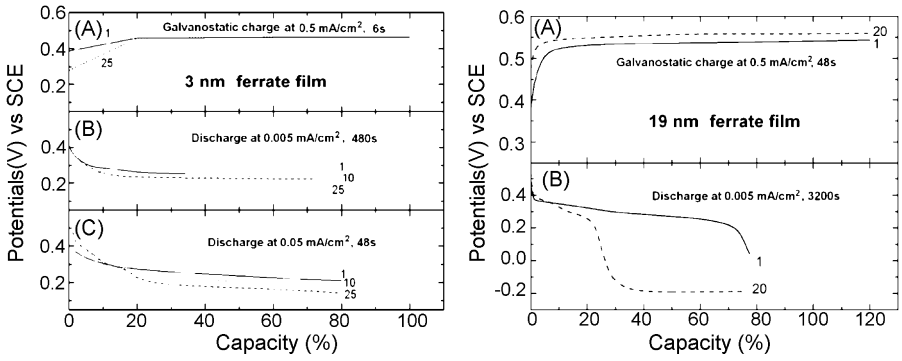

Fig. 3. Left: Quasi-reversible alkaline charge-transfer behavior of a thin ferrate film on Pt. The working electrode in this three electrode cell configuration is a 3 nm ferrate film on smooth Pt in 10 M NaOH. Charge/discharge cycles 1, 10, and 25 are indicated. Each cycle consists of (A) galvanostatic charge at 0.5 mA cm^{-2} for 6 s, followed by (B) discharge at 0.005 mA cm^{-2} for 480 s or (C) discharge at 0.05 mA cm^{-2} for 48 s. Right: Irreversible alkaline charge-transfer behavior of a thicker (19 nm) ferrate film on smooth Pt. Cell configuration and electrolyte are as described for the thinner (3 nm) film (for the left side of this figure). Charge/discharge cycles 1 and 20 are indicated. Each cycle consists of galvanostatic charge at 0.5 mA cm^{-2} for 48 s, followed by discharge at 0.005 mA cm^{-2} for 3200 s [30].

19 nm film rapidly passivates. Specifically, each film is repeatedly subject to a 0.5 mA cm^{-2} galvanostatic charge, followed by a deep 0.005 mA cm^{-2} galvanostatic discharge (to 80% of the Fe(VI/III) film theoretical, intrinsic $3e^-$ capacity). The 3 nm film smoothly approaches a plateau discharge potential between 0.2 and 0.3 V (left side of Fig. 3B). This contrasts with the discharge behavior of the 19 nm super-iron film (right side of Fig. 3B), in which this discharge plateau is only sustained during the initial portion of the discharge, after which the potential begins to sharply decline. A stable plateau between 0.38 and 0.2 V and a rapid polarization decay to −0.2 V was observed during the discharge of the 19 nm film. The plateau discharge potential was sustained to approximately 75% of the full capacity during the first cycle, and diminished to only 25% of this capacity within 20 cycles. Unlike the 19 nm film, the 3 nm film evidently sustained charge transfer reversibility at higher cathodic currents. Hence, as presented in the left side of Fig. 3C, at an order of magnitude higher discharge rate of 0.05 mA cm^{-2}, the 3 nm Fe(VI/III) film also sustains repeated, deep discharge. Compared to the 0.005 mA cm^{-2} cathodic cycling, by the 25th cycle, the polarization losses are higher at this higher current density. For example, in this last cycle, at 80% depth of discharge, the potential diminishes to 0.13 V versus SCE at 0.05 mA cm^{-2}, whereas the discharge potential is 90 mV higher at 0.005 mA cm^{-2}.

2.3. Conductive matrix facilitated Fe(VI/III) charge transfer

The conductive matrix to support Fe(VI/III) charge transfer, can be extended from a two dimensional structure to a high surface area three dimensional structure, by platinization of Pt and Ti substrates, or co-deposition of platinum and gold onto a Ti substrate, as detailed in reference [30]. The effective surface area of the platinized substrate increased with the degree of platinization. On a Pt substrate, up to a ∼1000-fold increase in electroactivity was obtained with 10.4 mg cm^{-2} of Pt deposit. On a Ti substrate, a normalized electroactivity of 326 was obtained when 4.5 mg cm^{-2} of Pt was loaded. By co-depositing Pt with Au on the Ti substrate, a stable surface containing up to 14 mg cm^{-2} of Pt with 15 mg cm^{-2} of Au deposit was achieved. The relationship between the normalized electroactivity and the amount of platinization on Pt or Ti substrate, as well as the preparation of Fe(VI/III) on these extended conductive matrix, were detailed in reference [30].

2.3.1. Platinum substrates for Fe(VI/III) charge transfer

A substantial improvement to sustain thick film charge transfer was observed when an extended conductive matrix was utilized as the film substrate. The left side of Fig. 4A summa-

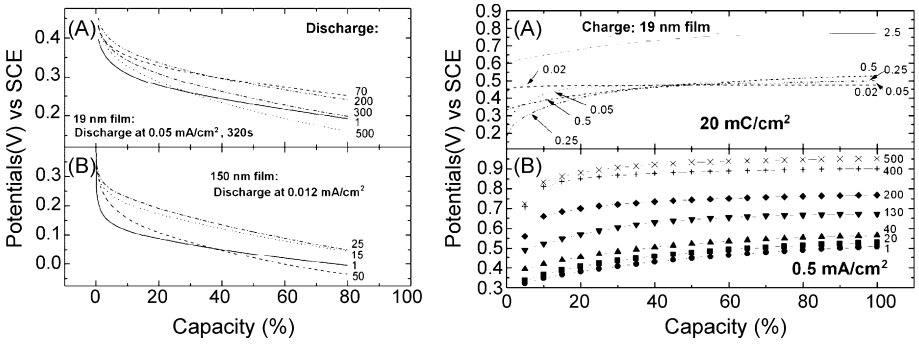

Fig. 4. Left: cathode discharge potential during cycling of (A) 19 nm and (B) 150 nm Fe(VI) film on a platinized Pt substrate (2.6 and 10 mg cm^{-2} of Pt load) in a galvanostatic configuration in 10 M NaOH. The cycling consists of galvanostatic charge at 0.5 mA cm^{-2} followed by galvanostatic discharge at 0.05 mA cm^{-2} for 320 s (19 nm) and at 0.012 mA cm^{-2} (150 nm). Right: cathode charging potential of a 19 nm film on a platinized (2.6 mg Pt cm^{-2}) Pt substrate: (A) for 20 mC cm^{-2} of charge, during the first cycle, at various current densities, (B) for various cycles at a fixed galvanostatic charge of 0.5 mA cm^{-2} for 40 s. The electrolyte used in half cell testing is 10 M NaOH [30].

rizes the discharge behavior during repeated charge/discharge cycles of a 19 nm super-iron film on platinized platinum, which contained 2.6 mg cm^{-2} of Pt deposit. Compared to the film on smooth platinum presented in the right side of Fig. 3, this film was able to sustain a substantially higher discharge current (0.05 compared to 0.005 mA cm^{-2}), as well as significantly higher reversibility (over 500 discharge cycles) without onset of significant passivation. As shown in the left side of Fig. 4B, a 150 nm super-iron film on a platinized platinum containing 10 mg cm^{-2} of Pt deposit can sustain over 50 charge/discharge cycles [30].

The right side of Fig. 4 summarizes the charging (the other half of the discharge/charge cycle) of the 19 nm Fe(VI/III) film on the extended conductive matrix. The right side of Fig. 4A compares the measured charging potentials over a range of applied galvanostatic oxidation current densities. As seen in the figure, charging potentials during the initial stages do not exhibit simple trends, and are observed to be significantly affected by cycle number, thickness, and current density. In the latter stages, a consistent increase of overpotential is observed with increasing charging current density. An order of magnitude increase in the relative charging current, to 0.25 mA cm^{-2}, generates only approximately ~40 mV charging overpotential. The next order of magnitude increase, to 2.5 mA cm^{-2}, incurs a substantially larger overpotential (~200 mV). For thicker super-iron films, a minimum current density of 0.5 mA cm^{-2} was useful to sufficiently regenerate at least 80% of the Fe(VI) discharge. To investigate both thin and thick super-iron films, a consistent charging current density of 0.5 mA cm^{-2} was utilized to facilitate oxidation of Fe(III) to Fe(VI), while sustaining relatively low charging overpotentials. The alkaline thermodynamic potential for oxygen evolution occurs at 0.16 V versus SCE, in accord with:

$$4OH^- \rightarrow O_2 + 2H_2O + 4e^-; \qquad E = 0.40\,\text{V vs.SHE} \qquad (1)$$

FeO_2^- species in NaOH were known to diminish the oxygen evolution potential by 0.1 V [37,38]. However, at room temperature, Pt exhibits a high overpotential to oxygen evolution, and below 0.5–0.6 V versus SCE, the rate of oxygen evolution is not significant [39]. Similarly no observable oxygen evolution was evident when charging the Fe(VI/III) films at these potentials. As can be seen in the right side of Fig. 4A, at charging currents $\leq$ 0.5 mA cm^{-2}, the charging potential is generally less than 0.5 V versus SCE. The super-iron films remained intact even after 500 cycles. In the right side of Fig. 4B, the limiting value of the charging potentials gradually increased with the increasing number of cycles and reaching a maximum of 0.95 V only at the end of 500 cycles [30].

In both cases, with or without the extended conductive matrix, thicker ferrate films exhibited greater overpotentials (lower cathode potentials) during discharge. This is observed by comparing A and B sections in the left side of Fig. 4. As seen in the figure, the final discharge potential was 0.0 V versus SCE for the thicker film (150 nm), but 0.15 V higher for the thinner film (19 nm) [30].

The importance of an effective, enhanced conductive matrix substrate was evident in attempts to obtain better reversibility with thicker (greater than 20 nm) super-iron films, as summarized in Table 1. When a 50 nm super-iron film was formed on a platinized Pt substrate with a normalized electroactivity of 550, the film passivated when discharged at a current density of 0.025 mA cm^{-2}, but discharged effectively at a current density of 0.012 mA cm^{-2}. In the latter case, the 50 nm film reversibly cycled 100 times before the onset of passivation. When a 50 nm super-iron film was deposited onto platinized Pt with a normalized electroactivity of 725, the film could sustain 100 cycles at a higher discharge current density of 0.025 mA cm^{-2}. Further enhancement in the conductive matrix also resulted in longer cycle life and 160 reversible cycles were sustained when the film was deposited onto a surface with a normalized electroactivity of 990 (discharged at a current density of 0.025 mA cm^{-2}). Greater reversibility was again observed when discharging at a lower current density, and the film sustained 250 cycles at a discharge current density of 0.012 mA cm^{-2} [30].

The formation of irreversible passivating Fe(III) centers is more likely in the case of thicker films. Consequently, this passivation results in the increased charge and discharge overpotentials, and restrains the super-iron film to discharge to a significant fraction of its intrinsic charge capacity. The facilitated super-iron charge transfer, upon platinization, as a result of the expanded conductive matrix to facilitate charge transfer is represented in Fig. 5. Without direct contact with the substrate, the shaded Fe(III) centers in the figure posed an impediment to charge transfer. This is partially (left side of Fig. 5) and fully alleviated (right side of Fig. 5), by the intimate contact with the enhanced conductive matrix, which maintains extended direct contact with the substrate [30].

2.3.2. *Platinized titanium substrates for Fe(VI/III) charge transfer*

Platinized Ti can also be used as the substrate for the reversible super-iron films. To effectively utilize super-iron films on platinized Ti substrates, it was observed that during the initial phases of cycling (for cycles 2 through 10) an extended charging time, equivalent to a 150% charge of the intrinsic capacity, was required, otherwise the full discharge could not

Table 1
Influence of normalized electroactivity and discharge current density on cycle life of a 50 nm film [30]

Normalized electroactivity	Current density (mA cm^{-2})	Depth of $3e^-$ discharge (DOD, %)	Cycles to polarization deactivation
550	0.012	75	100
725	0.025	80	100
725	0.012	80	250
990	0.025	80	160

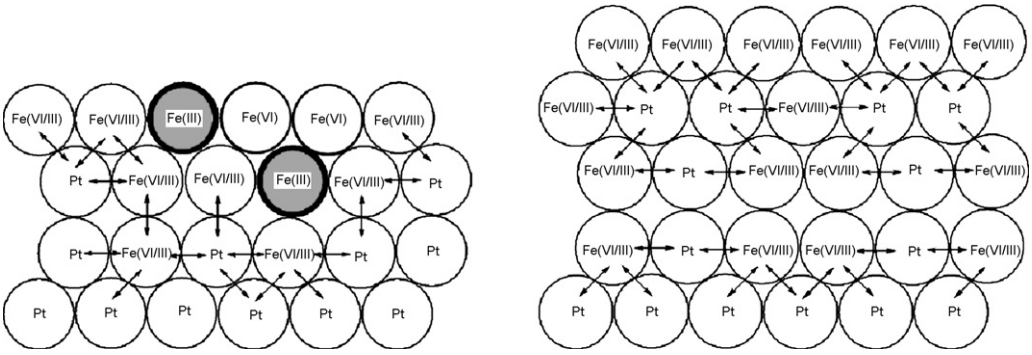

Fig. 5. Representation of partial (left side), and full (right side) alleviation of the Fe(VI/III) passivation in a ferrate film through an extended conductive matrix [30].

be accessed. Following this, the conventional charge (equivalent to 120% charge of the intrinsic capacity) was sufficient to sustain extended charge/discharge cycling. Initial morphological changes can occur in a high surface area, stressed, and crystallographically disordered platinized Pt surface [40,41]. The electronic changes associated with the formation of Ti-oxides may initiate this process [38]. This latter effect could arise from improved contact of the underlying Pt layer during cycling.

The charge/discharge curves of a 50 nm super-iron film on 7.5 mg Pt cm^{-2} platinized Ti are given in the left side of Fig. 6. One disadvantage encountered with the platinized Ti substrate is the difficulty to obtain larger amount of Pt deposits (over 7.5 mg cm^{-2} Pt deposits would result in an unstable powdery surface). Therefore, it was difficult to deposit more than 70 nm super-iron film on the platinized Ti [30]. However, a substantial improvement in the stability and upper thickness limit of the super-iron film was obtained when a Pt–Au co-deposited Ti was used as the substrate. A 300 nm super-iron film prepared on the Pt–Au/Ti substrate displayed a moderate cycle life of 20. Charge–discharge profiles are presented in the right side of Fig. 6.

2.4. Metal hydride anode compatibility with the rechargeable super-iron cathode films

Facilitated charge transfer Fe(VI/III) films compatibility with metal-hydride anodes was explored in conjunction with full cell charge storage [30]. Generally, metal hydride anodes are utilized in conjunction with the nickel oxyhydroxy (NiOOH) cathodes in alkaline media [42]. The half and full cell reactions in the charge storage process of a full super-iron/metal hydride cell can be described in an analogous manner to the NiOOH/metal hydride cell. During discharge, FeO_4^{2-} is reduced in the Na_2FeO_4 cathode and the metal hydride (MH_x) is oxidized to metal (M) in accordance with:

$$MH_x + xOH^- \rightarrow M + xH_2O + xe^-; \quad E = -0.82\,\text{V vs.SHE} \tag{2}$$

The process is reversed during the charge. Combined with the super-iron cathode reaction:

$$Na_2FeO_4 + 2H_2O + 3e^- \rightarrow 1/2Na_2Fe_2O_4 + NaOH + 3OH^- \tag{3}$$

The overall cell discharge reaction will be:

$$Na_2FeO_4 + 3/xMH_x \rightarrow 1/2Na_2Fe_2O_4 + 3/xM + NaOH + H_2O; \quad E = 1.42\,\text{V} \tag{4}$$

Interestingly, super-iron films deposited on extended conductive matrix substrates were characterized by a significantly longer cycle life in full metal hydride storage cells, compared to those measured in the half cell configuration [30]. In the cell, a 25 nm Fe(VI/III) film cathode, deposited on a 10 mg Pt cm^{-2}

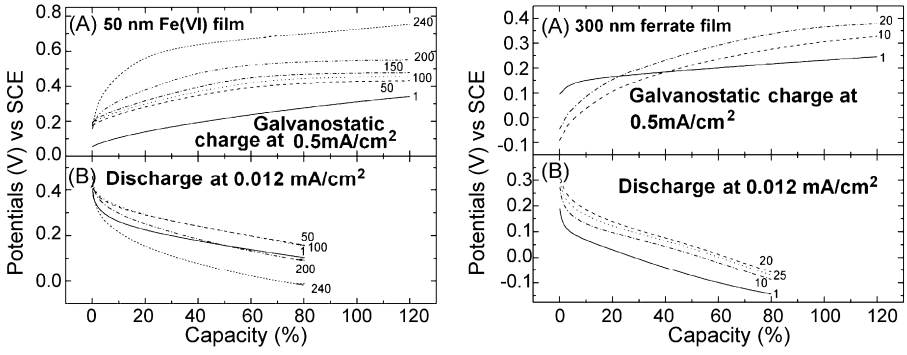

Fig. 6. Left: quasi-reversible alkaline charge transfer behavior of a 50 nm ferrate film on a platinized Ti (7.5 mg cm^{-2} of Pt load). (A) Galvanostatic charge at 0.5 mA cm^{-2}. (B) Galvanostatic discharge at 0.012 mA cm^{-2}. Right: quasi-reversible alkaline charge transfer behavior of a 300 nm ferrate film on a gold–platinum co-deposited Ti substrate (14 mg cm^{-2} of Pt and 15 mg cm^{-2} of Au loads). (A) Galvanostatic charge at 0.5 mA cm^{-2}. (B) Galvanostatic discharge at 0.012 mA cm^{-2}. The electrolyte used in half cell testing is 10 M NaOH [30].

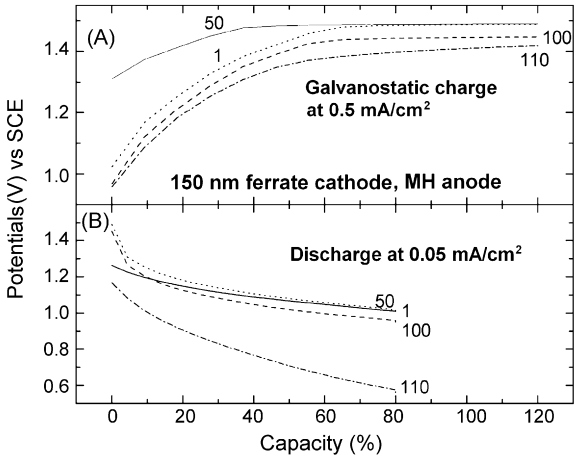

Fig. 7. Two electrode rechargeable behavior of 150 nm ferrate cathode (deposited on 10 mg cm^{-2} Pt platinized substrate) with a MH anode. (A) Full cell potential during a galvanostatic charge at 0.5 mA cm^{-2}. (B) Electrode film potential during a galvanostatic discharge at 0.05 mA cm^{-2}. The electrolyte used in full cell testing is 10 M NaOH [30].

platinized substrate, displayed high cell voltage. A discharge voltage of 1.2 V was sustained through the end of 300 cycles in the full cell, and within 0.22 V of the thermodynamic cell rest potential (Eq. (4)) [30].

Although the cycling of the cathode in the full cell was consistently higher than that of the similar half cell measurements, in both cases (full and half cell), as the thickness of the film increased, the cycle life decreased. The observed charge/discharge profiles of a 150 nm Fe(VI/III) film, in a super-iron metal hydride cell are presented in Fig. 7. Consistent with the prior half reaction measurements, the film was charged to 120% of its theoretical capacity at a constant current density of 0.5 mA cm^{-2}, and subsequently discharged to 80% at a constant current density of 0.05 mA cm^{-2}. As seen in the lower portion of the figure, in the first cycle, discharge commenced at ~1.3 V and decayed to 1.0 V at the end of the 80% capacity discharge. Subsequent to this initial cycle (through charge/discharge cycle 100), discharge commenced at a higher voltage of ~1.5 V. However, as seen in the figure, the discharge voltage decayed seriously after 100 cycles. A diminished voltage of 0.6 V was observed at the end of discharge in cycle 110. A 250 nm film, capable of storing 264 mC intrinsic capacity per cm^2, sustained stable and reversible charge storage only for 40 cycles. A 50% longer cycle life was achieved with metal hydride anode in comparison to the cycle life in the three electrode cell with a nickel counter electrode. This indicated a greater compatibility of the Fe(VI/III) film cathode with the metal hydride anode in the full cell [30].

3. Nonaqueous Fe(VI) charge transfer and super-iron lithium batteries

In this section, the cathodic chemistry of Fe(VI) compounds is considered in nonaqueous electrolytes for use as a lithium, or lithium-ion, anode electrochemical storage system. Primary nonaqueous super-iron/lithium battery is presented, and the initial results demonstrating reversibility of Fe(VI) cathodes in nonaqueous electrolyte system are also illustrated.

3.1. Primary nonaqueous super-iron battery

Licht's group introduced the utilization of Fe(VI) salts as a nonaqueous cathode, in conjunction with a lithium anode in nonaqueous media, in 2000 [9]. The Fe(VI) salts, such as $BaFeO_4$ and K_2FeO_4, are insoluble in a variety of organic solvents, including solvents conducive to studies of lithium electrochemistry such as acetonitrile (ACN), propylene carbonate (PC), ethylene carbonate (EC), γ-butyrolactone (BLA), and dimethoxyethane (DME). In addition, these Fe(VI) salts remain insoluble when necessary lithium salts are dissolved to increase the electrolytic conductivity. In the longest duration stability studies available, there is no Fe(VI) dissolution or reaction of either $BaFeO_4$ or K_2FeO_4 powders immersed in dry ACN, PC, DME, or BLA either with or without the dissolved lithium perchlorate. Insolubility and stability of Fe(VI) salts in nonaqueous electrolyte are attractive physical chemical properties for a nonaqueous super-iron battery.

Super-iron primary cells with a lithium anode were prepared in a conventional CR1216 coin cell case. The cathode composite was formed by mixing the indicated mass of Fe(VI) salt (either K_2FeO_4, $BaFeO_4$, $SrFeO_4$, or Li_2FeO_4) with the indicated weight percent of conductors (graphite or carbon black) or other additives. In each situation, the button cell was opened, the anode was retained, an appropriate electrolyte was added, and the new cathode was placed in the cell. Cells were discharged at a constant load. Cell potential variation over time was measured via LabView Data Acquisition on a PC, and cumulative discharge current (as mAh) was determined by subsequent integration.

In an alkaline super-iron battery, Fe(VI) cathodes discharge through a three-electron electrochemical reduction reaction. The cathodic discharge mechanism of Fe(VI) in nonaqueous super-iron battery is complex. In 2000, Licht's group noted that the Fe(VI) discharge in nonaqueous media was consistent with the storage of three electrons per Fe center, and consistent with other nonaqueous cathodes, suggested a mechanism of charge transfer via the insertion of Li^+ (Another more recent, alternate mechanism will be presented later in this section) [9]

$$MFeO_4 + xLi^+ + xe^- \rightarrow Li_xMFeO_4$$

$$M = K_2, Ba, Sr, Li_2, \text{etc.} \quad (5)$$

Nonaqueous primary super-iron batteries were initially investigated with Fe(VI) cathodes comprised of either Li_2FeO_4, K_2FeO_4, $SrFeO_4$ or $BaFeO_4$. The 601 mAh g^{-1} theoretical charge capacity of Li_2FeO_4 based on the insertion of three Li^+ per Fe, is substantially higher than the 406 mAh g^{-1} for K_2FeO_4, 388 mAh g^{-1} for $SrFeO_4$, and 313 mAh g^{-1} for $BaFeO_4$. Fig. 8 compares the discharge of Li_2FeO_4, K_2FeO_4, $SrFeO_4$, and $BaFeO_4$ cathode super-iron lithium batteries with a LiTFB PC:DME electrolyte. Under equivalent conditions, the $BaFeO_4$ cathode exhibits lower polarization losses and a higher Faradaic efficiency (based on equivalents of Li^+ insertion per equivalent

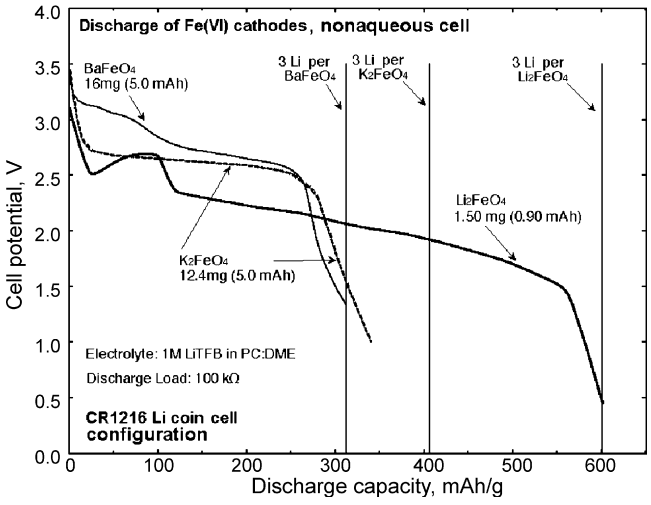

Fig. 8. Constant load discharge of cells containing a Li_2FeO_4, K_2FeO_4, $SrFeO_4$, or $BaFeO_4$ Fe(VI) cathode and a lithium anode. Electrolyte is 1 M LiTFB PC:DME [9].

of Fe(VI)) than the K_2FeO_4 cathode. However, due to its lighter mass the observed specific capacity of the K_2FeO_4 is marginally higher. The lower discharge voltage of the lithium, compared to barium, strontium or potassium super-iron cathodes is likely due to the lower purity and resultant higher polarization of this cathode. Note that unlike K_2FeO_4, $SrFeO_4$, or $BaFeO_4$, the measured purity of the Li_2FeO_4 is very low (~20%), requiring 7.5 mg of salt to provide the indicated 1.5 mg of Li_2FeO_4 in the cathode, and the mass normalized measured capacity is based on this small active component of this impure material.

The configuration of the primary super-iron/Li batteries were studied to enhance nonaqueous Fe(VI) cathodic charge transfer for both K_2FeO_4 and $BaFeO_4$ cathodes. Table 2 presents solvent and electrolyte effects on the cathodic charge capacity of a $BaFeO_4$ cathode [21].

Table 2
Variation of the $BaFeO_4$ cathodic capacity with electrolyte supporting salt or with electrolyte solvent

Solvent	Supporting salt	Average potential (V)	Capacity ($mAh\,g^{-1}$)
Acetonitrile	$LiClO_4$	2.29	28
Acetonitrile	LiTFMS	2.50	30
Acetonitrile	$LiBF_4$	2.49	38
Acetonitrile	$LiPF_6$	2.15	56
EC–DEC	$LiClO_4$	2.50	84
EC–DEC	LiTFMS	2.23	26
EC–DEC	$LiPF_6$	2.13	48
γ-BLA	$LiClO_4$	2.64	113
γ-BLA	LiTFMS	2.26	59
γ-BLA	$LiBF_4$	2.18	78
γ-BLA	$LiPF_6$	2.52	206
PC–DME	$LiClO_4$	2.65	241
PC–DME	LiTFMS	2.41	129
PC–DME	$LiBF_4$	2.67	247
PC–DME	$LiPF_6$	2.57	260

Lithium salts used in electrolyte are 1 M concentration [21].
Note: Cathodes are composed of 80 wt% BaFeO4 and 20 wt% carbon black, with capacity determined as BaFeO4 mass normalized mAh of discharge measured to 2 V. The cell is discharged over a 67 kΩ load at 25 °C. The tabulated potential is measured as the average discharge potential through a cutoff voltage of 2 V.

As summarized, the specific capacity of $BaFeO_4$ increased from 28, 84, 113, to 241 $mAh\,g^{-1}$ when the solvents for 1 M $LiClO_4$ electrolyte was changed from acetonitrile, 1:1 (v/v) EC–DEC, γ-BLA to 1:1 (v/v) PC–DME, respectively. In addition to the solvent, the variation of the electrolyte supporting salt also has a substantial effect on Fe(VI) cathodic capacity. As summarized in the table, in a range of solvents, dissolved LiTFMS did not effectuate charge transfer as efficiently as $LiClO_4$, which in turn did not promote the high degree of cathode capacity observed in Fe(VI) cells with the $LiBF_4$ and $LiPF_6$. As also evident from the table, an electrolyte prepared with a PC–DME co-solvent yields higher $BaFeO_4$ capacity (260 $mAh\,g^{-1}$ in 1 M $LiPF_6$) than the other studied solvents, although the γ-BLA solvent was also effective (206 $mAh\,g^{-1}$ with 1 M $LiPF_6$).

Fig. 9a presents in a PC–DME electrolyte prepared with a range of lithiated and nonlithiated supporting salts, the nonaqueous discharge of cells containing a $BaFeO_4$/carbon black cathode. Nonlithium electrolytes cells may exhibit significantly impaired cathodic charge transfer. In these electrolytes, the only lithium ion source is the buildup that occurs during mass transport from the discharging anode. This impaired cathodic charge transport is clearly evident in Fig. 9a, and seen as the low cathodic specific capacity measured during discharge of the lithium free TEA-PF_6 (tetraethyl ammonium hexafluorophosphate) and TEA-TFB (tetraethyl ammonium hexafluorophosphate) PC–DME electrolytes. For the lithiated salt PC–DME electrolytes, the highest cathodic capacity was measured for the 1 M $LiPF_6$ electrolyte [21].

While $LiPF_6$ supported higher cathodic capacities in Fe(VI) cells, $LiBF_4$ facilitated better charge transfer. This is indicated by the lower $LiPF_6$ plateau discharge potential in Fig. 9a. The inset of Fig. 9a also shows this facilitated charge transfer, that there is a lower polarization in the 1 M $LiBF_4$ compared to the steep polarization losses in the 1 M $LiPF_6$ electrolyte (polarization of 3.0 $mV\,\mu A^{-1}\,cm^2$ versus 5.7 $mV\,\mu A^{-1}\,cm^2$ in $LiPF_6$). These polarizations represent charge transfer rates which are low compared to the equivalent aqueous Fe(VI) systems. For example, polarization losses are several orders of magnitude smaller for the three electron Faradaic reduction of aqueous alkaline $BaFeO_4$ cathodes, and in this aqueous media, Fe(VI) has been observed to sustain levels of cathodic charge transfer at ampere, rather than milliampere, currents. Interestingly, as also seen in the inset of Fig. 9a, a lithium iodide electrolyte considerably decreases polarization losses to 0.6 $mV\,\mu A^{-1}\,cm^2$, albeit at a lower onset potential of 3.0 V versus 3.5 V observed for the $LiBF_4$ electrolyte [21].

Polarization toward nonaqueous cathodic charge transfer can be expected to be affected by modifications of the cathode's supporting conductive matrix. Also, polarization losses should decrease for smaller cathode particle size, and with an increase in the discharge temperature. In Fig. 9b, with variation of the constant load during the 25 °C discharge, the need for improved cathodic charge transfer is evident in the 1 M $LiBF_4$ PC–DME electrolyte 80% $BaFeO_4$ (<150 μm particle), 20% carbon black cathode cell. In the figure, compared to the 67 kΩ load, the lighter

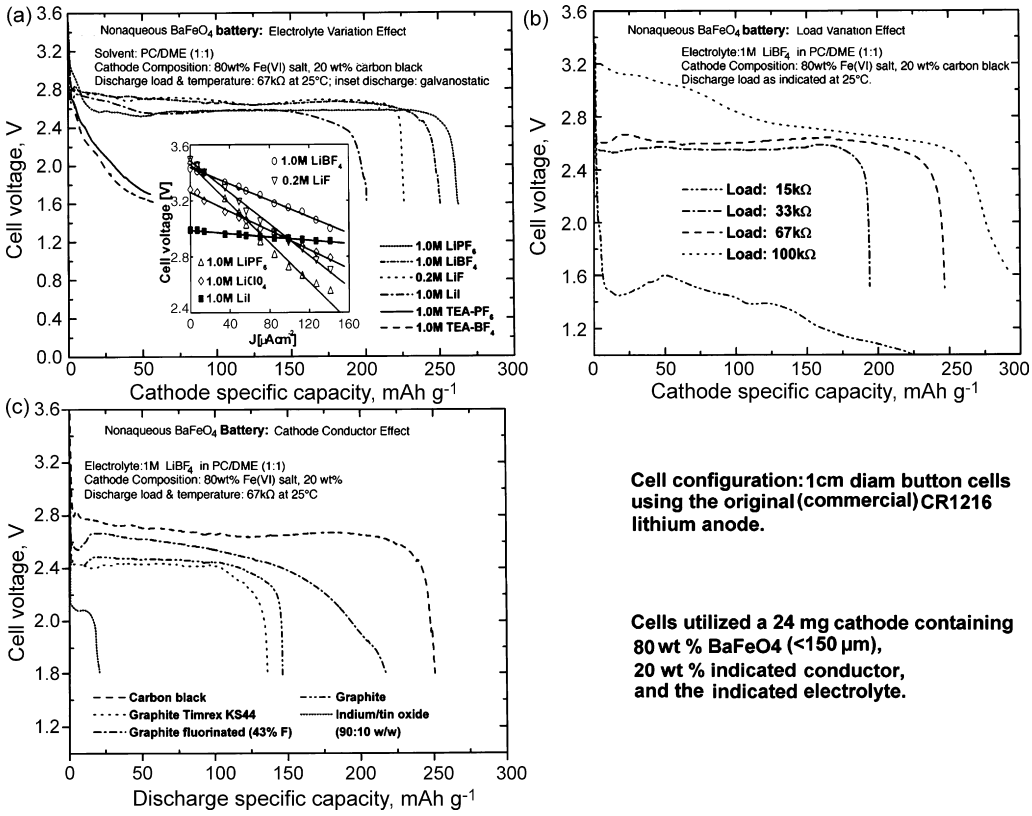

Fig. 9. (a) Electrolyte effect on the $BaFeO_4$ cathode capacity in Li anode cell discharged with PC/DME electrolytes containing a variety of different salts. Inset: polarization measured as a function of potential measured with constant current at 25 °C. Conductor: carbon black; discharge load: 67 kΩ. (b) Constant load variation effect on $BaFeO_4$ cathode capacity in Li anode cell with 1 M $LiBF_4$ PC/DME electrolyte. Conductor: carbon black. (c) Cathode conductive matrix effect on $BaFeO_4$ cathode capacity in Li anode cells with 1 M $LiBF_4$ PC/DME electrolyte. Discharge load: 67 kΩ [21].

100 kΩ load discharge substantially increased the average cell potential and increased specific capacity by over 10%. The cathode capacity fell substantially for discharge at high rates, such as during the 33 kΩ discharge, and this cathode/electrolyte configuration did not support even higher rate discharge. As seen in the figure, the cell potential did not recover during cell discharge at 15 kΩ [21].

Fig. 9c explores the effects of variations of the cathode conductive additive in nonaqueous media. For the 1 M $LiBF_4$ PC–DME $BaFeO_4$ cell, discharge was particularly ineffective for the non-carbon conductor (indium tin/oxide, ITO). Replacement of the 20 wt% carbon black by an equal mass of 1 μm graphite in the $BaFeO_4$ cathode mix lowered the capacity from 247 to 196 mAh g^{-1}. Of the Fe(VI) 20 wt% additives investigated, carbon black consistently supported the highest cathodic capacity, both in fluorinated and non-fluorinated electrolytes, or when compared to fluorinated graphites [21].

Decrease of the cathode salt particle size can substantially increase the interfacial surface area, and in principal can improve electrolytic mass diffusion and diminish the solid state diffusion path length. As summarized in Table 3, the decrease of Fe(VI) salt particle size improved the Fe(VI) cathode specific storage capacity. In the 1 M $LiPF_6$ PC–DME electrolyte, the decrease of $BaFeO_4$ particle size from 111 to 54 μm, or <35 μm increased cathode capacity, respectively, from 241 to 252, or 290 mAh g^{-1} [21].

It is likely that the Fe(VI) cathode will exhibit further improvements in cathodic charge transfer with further optimization of the Fe(IV) particle morphology, and a further enhancement of cathodic charge transfer can occur with the increase of discharge temperature. This activation was observed for the smallest particle range explored <35 μm $BaFeO_4$; as also included in Table 3, this exhibited increased cathodic capacity to 298 mAh g^{-1} with increase of discharge temperature from 25 to 50 °C [21].

Table 3
Variation of the $BaFeO_4$ cathodic capacity with either temperature or $BaFeO_4$ particle size [21]

Temperature (°C)	Particle size (μm)	Average potential (V)	Capacity (mAh g^{-1})
25	<150	2.57	260
25	73–149	2.68	241
25	35–73	2.62	252
25	<35	2.62	290
0	<35	2.56	15
25	<35	2.62	290
40	<35	2.73	295
50	<35	2.63	298

Note: Cathodes with the indicated particle size BaFeO4 are composed of 80 wt% BaFeO4 and 20 wt% carbon black. The cells use 1 M LiPF6 in (1:1, v:v) PC/DME, electrolyte, and are discharged over a 67 kΩ load at the indicated temperature.

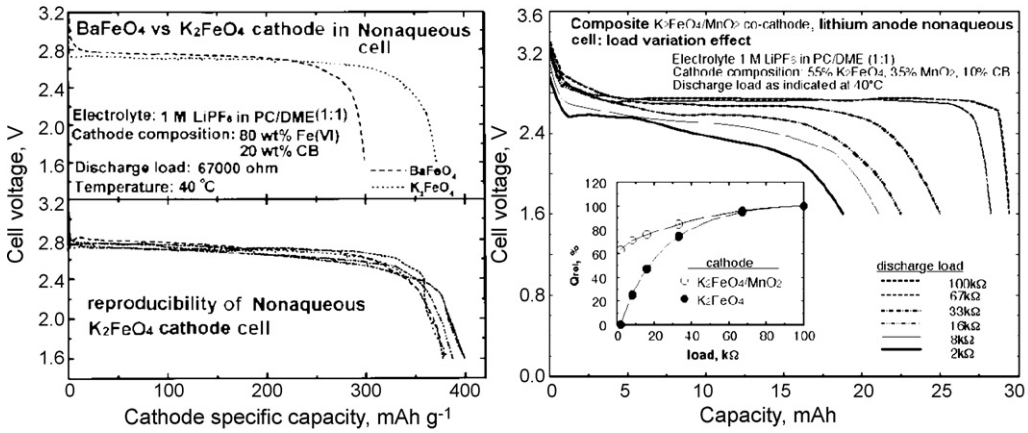

Fig. 10. Left: Fe(VI) cathode/Li anode cells with 1 M $LiPF_6$ PC/DME electrolyte. Top: the specific cathode capacity of 24 mg cathodes containing 80 wt% K_2FeO_4 or $BaFeO_4$ (small particle <35 μm diameter salt) and 20 wt% carbon black. Bottom: K_2FeO_4 cathode discharge reproducibility. Right: discharge of Fe(VI)/MnO_2 co-cathode/Li anode cells with PC/DME electrolyte. The cathode comprises 100 mg dry mass of cathode (100 mg total mass of K_2FeO_4, MnO_2 and CB) to balance the available anode capacity of 29 mAh. Cells are discharged at 40 °C utilizing the indicated constant load [21].

The top portion of Fig. 10 left compares the specific cathode capacity of small particle (<35 μm) K_2FeO_4 or $BaFeO_4$ cathodes. The combined benefits of the smaller particle size, change of supporting salt and increased discharge temperature also result in a significant increase in specific capacity for the K_2FeO_4 cathode (up to 370 mAh g^{-1}, compared with 290 mAh g^{-1} shown in Fig. 8).

In an aqueous system, MnO_2 substantially enhanced Fe(VI) charge transfer resulting in a synergistic increase in charge storage for a Fe/Mn co-cathode salt [19]. As seen in the right side of Fig. 10, a nonaqueous co-cathode consisting of K_2FeO_4 and lithiated MnO_2 also provided an effective cathode. As observed, the co-cathode cell discharged to the same capacity but utilizing only 100 mg of the cathode compared to 153 mg in the original lithiated MnO_2 cell. Hence the co-cathode has significantly higher capacity than the MnO_2 cathode (without K_2FeO_4). The right side of Fig. 10 inset shows the relative capacities for Fe(VI) and Fe(VI) co-cathode cells. In this determination, discharge capacity was measured to 2 V, and relative capacity was calculated and normalized to the capacity measured in discharge of the 100 kΩ load cell. The co-cathode used was as described above, while the Fe(VI) cathode cell contained only K_2FeO_4 and carbon black (without lithiated MnO_2). In particular, inclusion of MnO_2 as a co-cathode facilitates the cathode discharge. It is evident from the figure inset, that under equivalent heavy loads, the co-cathode discharged to a significantly higher storage capacity than the Fe(VI) cathode alone [21].

3.2. Electrochemical behavior of Fe(VI) in nonaqueous electrolyte and reversible super-iron/Li batteries

As presented at the beginning of this section, the Fe(VI) storage mechanism for cell discharges in Li containing nonaqueous media had been considered as the intercalation and insertion of Li^+. However, the more recent evidence suggests that the iron centers undergo a partially reversible Faradaic reduction in the compounds from 6^+ to 3^+ states, central to this interpretation is direct Mössbauer measurement of the iron valence state of the cathode during charge storage [32].

Fig. 11 shows typical cyclic voltammograms (CVs, experimental details are in reference [32]) of composite electrodes comprising K_2FeO_4 or $BaFeO_4$, carbon black (CB) and polyvinyldene difluoride (PVDF), in PC–$LiClO_4$ solution.

These voltammograms show that both compounds, K_2FeO_4 and $BaFeO_4$, are electrochemically active. A reduction process is clearly seen in the 1.5–2.5 V (Li/Li^+) range for K_2FeO_4 and in the 2–3 V range for $BaFeO_4$, with corresponding oxidation processes at around 3–4 V and 3.5–4 V, respectively. The broad peaks with the large hysteresis between the cathodic and anodic peaks (1.5 V) indicate that the electrochemical process is complex and suffers significant kinetic limitations. $BaFeO_4$, however, shows a slightly smaller hysteresis than K_2FeO_4 during lithiation and delithiation processes, although the cathodic and anodic peaks of the CVs of $BaFeO_4$ electrodes are also broad. Adding larger amounts of carbon additive to the composite electrodes leads in both cases (K_2FeO_4 and $BaFeO_4$ electrodes) to a decrease in the hysteresis between the cathodic and anodic peaks. 20%, rather than 10%, carbon black in a $BaFeO_4$ electrode results in a 2-fold increase of the observed electrode capacity (100 instead of 50 mAh g^{-1}) [32].

The electrochemical response of the nonaqueous Fe(VI) cathodes reflects several kinetic challenges related to both the intrinsic properties of the active mass, and to the electrical contact among the particles. For example, there is a positive shift of the anodic peak in the CVs of the composite K_2FeO_4 electrodes when the amount of the carbon black is increased from 10 to 20 wt% and the active mass is lowered accordingly to 70 from 80 wt% (Fig. 11). In parallel, the specific capacity of the active mass is higher for the electrode comprising 70 wt% active mass, probably due to the higher amount of carbon black which improves the interparticle electrical contact. These electrodes (70 wt% active mass) reach their maximal capacity during cycling faster than electrodes comprising of higher active mass but lower carbon content. The electrochemical activity of these electrodes does not appear to be affected by solution reactions,

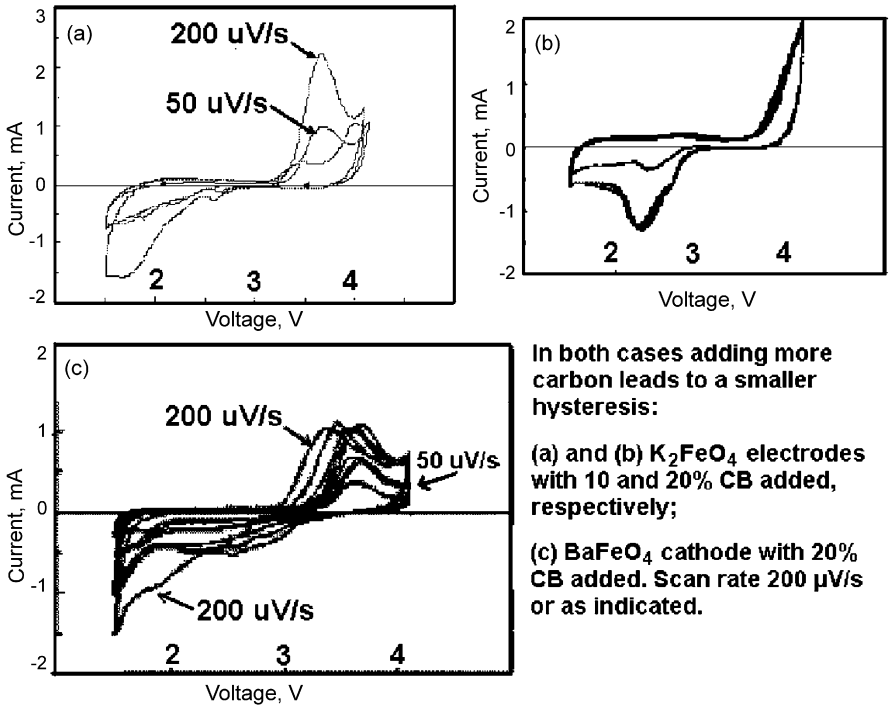

Fig. 11. CV of K_2FeO_4 and $BaFeO_4$ cathodes with different amounts of added carbon [32].

and the charge storage reactions occur within the known electrochemical window of the electrolytic solutions. The highest capacity for K_2FeO_4 composite electrodes was observed with 10 wt% carbon black. For further investigations, 20 and 10 wt% carbon black for $BaFeO_4$ and K_2FeO_4 electrodes, respectively, were chosen as optimal [32].

Fig. 12a and b shows typical chronopotentiograms of K_2FeO_4 and $BaFeO_4$ composite electrodes, respectively, in repeated galvanostatic cathodic and anodic polarization in EC–PC 1:1/$LiClO_4$ 1 M and $LiAsF_6$ 1 M THF solutions, as indicated. Results from different solutions are also presented to demonstrate that the role of the electrolyte solution used is minor. The sloping potential profiles in the range of 3–1.5 V for the cathodic processes and 2.5–4 V for the anodic processes correspond to the broad peaks that characterize the voltammetric response presented in Fig. 11. Elemental analysis of cycled electrodes using atomic absorption (AA, experimental details are in reference [32]) shows that lithium is inserted into the active mass in amounts corresponding to the charge measured. Hence, the electrochemical processes presented in Figs. 11 and 12 are consistent with the lithiation and delithiation of the electrodes studied [32]. Anodic polarization does not remove all the lithium from the active mass, as can be seen by a comparison of the charge involved in the first cathodic polarization and that related to the first anodic process and subsequent cycles and the corresponding element analyses.

Fig. 13a shows the cathodic capacity versus cycle number (galvanostatic charge–discharge cycling) of K_2FeO_4 electrodes containing different amounts of carbon, as indicated. As seen in this figure, it takes the electrodes a few cycles to reach a maximal capacity close to the theoretical value (~310 mAh g^{-1}), depending on the electrode's composition. The capacity then fades from cycle to cycle and stabilizes at a low value (approximately 1/3 of the theoretical capacity). These electrodes could be cycled reversibly hundreds of times in the alkyl carbonate-based solutions, showing low (100 mAh g^{-1}) but stable capacity. Similar capacity curves (Fig. 13b) for $BaFeO_4$ electrodes start from the highest values (above 200 mAh g^{-1}) in the first cycle,

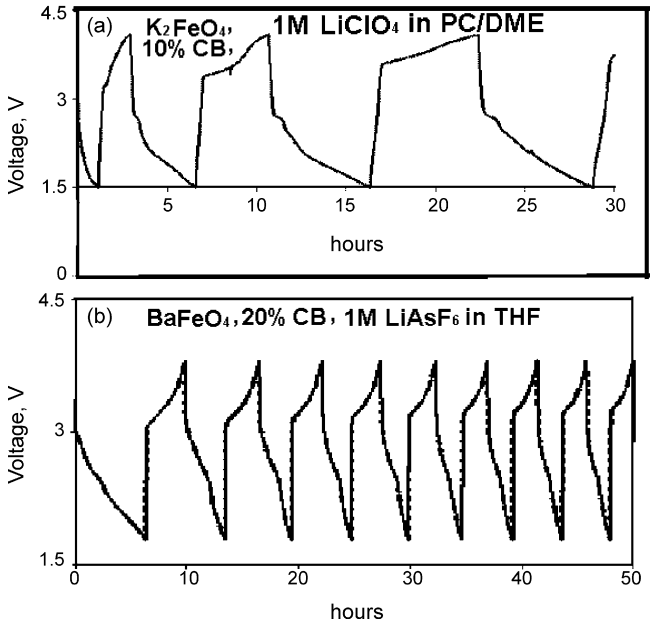

Fig. 12. (a) A typical chronopotentiogram of a K_2FeO_4 composite electrode, 10% CB, 10% PVDF, cycled in a coin-type cell in a $LiClO_4$ 1 M PC/DME solution. (b) A typical chronopotentiogram of a $BaFeO_4$ composite electrode, 10% CB, 10% PVDF, cycled in a $LiAsF_6$ 1 M THF solution. Galvanostatic cycling at *C*/10 rates [32].

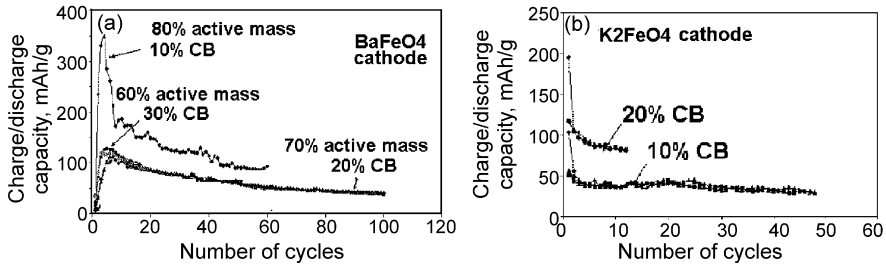

Fig. 13. (a) Charge and discharge capacity vs. cycle number of composite $BaFeO_4$ electrodes with 10, 20, and 30% of carbon black. (b) Charge and discharge capacity vs. cycle number of composite K_2FeO_4 electrodes with 10 and 20% of carbon black [32].

and then the capacity decreases slightly, but monotonously, until stabilization at approximately 80–100 mAh g^{-1}. Note that during the first cycle of $BaFeO_4$ electrodes, the charge that relates to the first lithiation process is higher than that of the following delithiation process [32].

Table 4 summarizes a series of electrochemical measurements carried out with different $MFeO_4$ composite electrodes (cycled versus Li counter electrodes in coin-type cells).

Table 5 summarizes the elemental analysis of composite $BaFeO_4$ composite electrodes by atomic absorption (AA). The relative amounts of lithium and iron were analyzed in order to measure the stoichiometry of the lithiated compounds at different stages of their lithiation–delithiation process. The relevant capacities were measured electrochemically and are also listed. As seen in Table 5, the lithium content of electrodes that underwent cathodic polarization as a single step, measured by AA, was always lower than what would be expected from the charge measurements. This is consistent with either the occurrence of side reactions, which do not involve lithiation (e.g., solvent reduction that forms solution species), or a partial self-discharge of the lithiated electrodes, as they are disconnected from the potentiostat at the low potential. Oxidation/delithiation of these electrodes leaves an appreciable amount of lithium trapped in the electrodes, as measured by both electrochemical and elemental analysis. For electrodes that underwent a lithiated–delithiated cycle, there is a good match between the AA data and the charge measurements. This supports the assumption that the lithiated electrodes show lower lithium content than the corresponding charge measured, due to some delithiation occurring during the treatment [32].

There is evidence from elemental analysis for dissolution of K^+ ions from K_2FeO_4 electrodes into $LiClO_4$ 1 M EC/DME solutions. No dissolution of Fe ions could be detected. Hence, it is suggested that some K^+ ions are substituted by Li^+ ions in the active mass [32].

Unlike thicker films, thin Fe(VI/III) films exhibit extensive, high-capacity nonaqueous rechargeablity (over 300 mAh g^{-1} capacity for $\gg$50 charge/discharge cycles). Reversibility of the electrodes was also probed using thin films of K_2FeO_4 on Pt foils in a PC/DME 2:1 1 M $LiClO_4$ electrolyte [32]. The electrodes

Table 4
Summary of galvanostatic measurements of various $MFeO_4$ salts [32]

Type of electrode	Electrolyte	General electrochemical behavior	Capacity and capacity fading
$BaFeO_4$; 10%, 20% CB; 10%, 20% KS6; 10% KS6–10% CB	$LiClO_4$–1 M-EC/PC, $LiAsF_6$–1 M-THF, $LiAsF_6$–2 M-THF, $LiAsF_6$–1 M-DMC	Good reversibility at prolonged charge/discharge processes. Evident hysteresis between cathodic and anodic processes.	About 200 mAh g^{-1} in the first lithiation. Sustain about a 90 mAh g^{-1} steady capacity during hundreds of cycles.
K_2FeO_4; 10%, 20% CB	$LiClO_4$–1 M-EC/PC, $LiAsF_6$–1 M-THF, $LiAsF_6$–2 M-THF, $LiAsF_6$–1 M-DMC	Good reversibility at prolonged charge–discharge processes. Capacity increases to a peak value and then fades to a stabilized low value.	About 310 mAh g^{-1} in the first lithiation. Sustain about a 85 mAh g^{-1} steady capacity during hundreds of cycles.
Sr_2FeO_4; 10%, 20% CB	$LiClO_4$–1 M-EC/PC	Poor reversibility, low capacity	Less than 20 mAh g^{-1}

Table 5
Correlation between charge measured (chronopotentiometry) and Li content (atomic absorption, AA) of $BaFeO_4$ electrodes during first lithiation and first lithiation–delithiation cycle [32]

Electrochemical process	Capacity measured during first lithiation (mAh g^{-1})	Capacity measured during first delithiation (mAh g^{-1})	Capacity measured from AA (mAh g^{-1})
Slow polarization to 1.5 V at *C*/45 rates	236.5	Not measured	177.37
Slow polarization to 1.5 V at *C*/45 rates	180	Not measured	154.41
Slow polarization to 1.5 V at *C*/45 rates	207	Not measured	140.85
Slow polarization to 1.5 V at *C*/45 rates	207	Not measured	125.2
Slow polarization to 1.5 V and then to 4 V at *C*/45 rates	222.6	104.33	112.47
Slow polarization to 1.5 V and then to 4 V at *C*/45 rates	236.4	111.28	121.46

Table 6
Summary of Mössbauer spectroscopy analysis of $BaFeO_4$ electrodes [32]

Type of process $LiClO_4$ 1 M PC–DME 2:1 solution	Measured capacity during electrochemical reduction and oxidation processes (mAh g^{-1})	Percentage of Fe^{6+} (%)	Percentage of Fe^{3+} (%)
Polarization to 1.8 V and then to 4 V at *C*/45 rate.	Reduction, 68; Oxidation, 30	89	11
10 complete cycles in the 1.8–4 V range and removed at 1.8 V, *C*/45 rate.	Average of charge–discharge capacity, 35	83	17
One reduction/oxidation cycle, 1.5–4 V range, at *C*/45 and removed at 3 V.	Average of charge–discharge capacity, 35	83	17
Slow polarization to 1.8 V at a *C*/45 rate.	Reduction, 85	79	21
20 complete cycles in the 1.8–4 V potential range and removed at 3 V.	Average of charge–discharge capacity, 37	83	17
$BaFeO_4$ pristine electrode		92	8

were galvanostatic cycled at *C* rates (i.e., the entire capacity was discharged and charged during less than 1 h per process). In these experiments, the complications related to the composite structure of the usual electrodes were eliminated, and hence, the intrinsic behavior of the active mass could be better examined. As seen in Fig. 14a, K_2FeO_4 thin-film electrodes could be cycled reversibly at a capacity above 300 mAh g^{-1} with a little capacity fading during prolonged cycling. The fact that the discharge capacity is slightly higher than the charge capacity can be explained by the reduction of PC at the lowest potentials that the electrodes reach in these experiments (1.5 V versus Li/Li^+) [43]. As seen from the potential profiles in Fig. 14b (galvanostatic cycling in the $LiClO_4$ 1 M PC/DME solution), there are two processes during the oxidation of the thin film electrode. This phenomenon was explained that Fe(VI) compounds are reformed possibly by a two-step process via a Fe^{4+} intermediate [32].

Mössbauer spectroscopy confirmed that cathodic polarization (lithiation) of K_2FeO_4 changes the oxidation state of the iron from 6^+ to 3^+, and that the reverse anodic process (delithiation) of the reduced material regenerates an iron 6^+ compound. The Mössbauer spectroscopic measurements provided direct evidence that the corresponding cathodic and anodic processes of these compounds, as described above (Figs. 11–14), involve a reversible change in the oxidation state of the central iron atoms of the active materials. The Mössbauer spectroscopic measurements showed similar changes in the oxidation state of iron during galvanostatic cycling of $BaFeO_4$ composite electrodes. The data related to the Mössbauer spectroscopic measurements of composite $BaFeO_4$ electrodes are summarized in Table 6. In general, there is a correlation between the electrochemical charge measurement and the quantitative analysis of the Mössbauer spectroscopy. Cathodic polarization transforms Fe^{6+} to Fe^{3+}, while a consecutive polarization reforms the Fe^{6+}. It can be clearly seen that about 17% Fe^{6+} of the active electrode decomposed or underwent irreversible changes during prolonged cycling in several experiments [32].

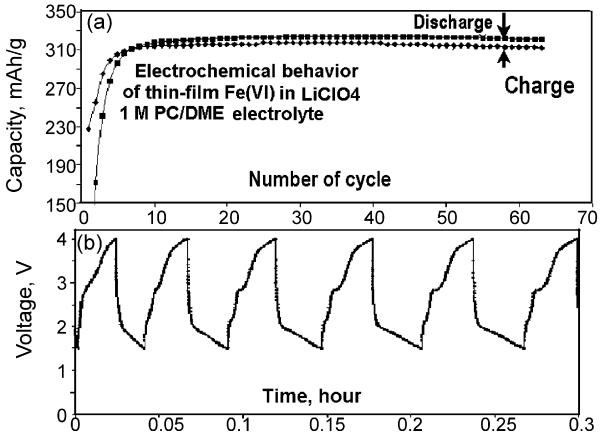

Fig. 14. The electrochemical behavior of a thin film K_2FeO_4 on a Pt electrode. The thin film is cycled in a $LiClO_4$ 1 M PC/DME 2:1 solution: (a) charge and discharge capacity vs. cycle number (galvanostatic cycling at *C*/10 rates) and (b) typical potential profile of these electrodes upon galvanostatic cycling [32].

The results above show that the Fe(VI) compounds can be electrochemically reduced and re-oxidized in nonaqueous Li salt solutions. The charge/discharge process of Fe(VI)/Fe(III) in nonaqueous medium involves both the lithiation/delithiation of the active mass and the reduction/oxidation of the iron (from 6^+ to 3^+ or from 3^+ to 6^+ states; confirmed by atomic absorption, Mössbauer spectroscopy, and charge measurements in the electrochemical processes) [32].

4. Summaries

Three super-iron battery types: super-iron rechargeable alkaline batteries, super-iron primary lithium batteries and super-iron rechargeable nonaqueous batteries, are presented.

Reversible Fe(VI) chemistry was developed with Fe(VI/III) thin film cathode. High-capacity Fe(VI/III) films were deposited by electrochemical reduction of Na_2FeO_4 with an intrinsic $3e^-$ cathode storage of 485 mAh g^{-1}. Films were alternatively deposited on either smooth conductive substrates or on extended conductive matrixes composed of high-surface-area Pt, Ti and Au. Whereas ultra-thin (e.g., 3 nm) Fe(VI/III) film exhibited a high degree of reversibility, thicker films were increasingly passive toward the Fe(VI) charge transfer. The extended conductive matrix facilitated a 2 orders of magnitude enhancement in charge storage for reversible Fe(VI/III) super-iron thin films. A 100 nm Fe(VI) cathode on the extended conductive matrixes sustained 100–200 reversible three-electrode charge/discharge cycles, and a 19 nm thin film cathode sustained 500 such cycles. In conjunction with a metal hydride anode, a 250 nm super-iron film cathode film sustained 40 charge/discharge cycles, and a 25 nm film was reversible throughout 300 cycles.

Super-iron cathodes can also be discharged in conjunction with a Li anode in nonaqueous media. Optimization of the nonaqueous primary super-iron/Li batteries was summarized.

Through proper selection of electrolytes, use of carbon black as the conductor, reduction of cathode particle size, and moderate increase of temperature (from room temperature to 40 °C), the cathodic charge transfer of Fe(VI) in nonaqueous electrolyte was enhanced. Co-cathodes comprised of K_2FeO_4 and MnO_2 exhibited high storage capacity.

Fe(VI) cathodes also exhibited reversibility in nonaqueous batteries. The charge/discharge process of Fe(VI)/Fe(III) in a nonaqueous medium involved the lithiation/delithiation of the active mass and the reduction/oxidation of the iron (from 6^+ to 3^+ or from 3^+ to 6^+ states). However, similar to that in the aqueous system, only the thin film Fe(VI) electrodes could sustain high reversibility involving the full theoretical capacity in nonaqueous battery system.

References

[1] Y. Lee, I.H. Um, J. Yoon, Environ. Sci. Technol. 37 (2003) 5750.
[2] V.K. Sharma, Adv. Environ. Res. 6 (2002) 143.
[3] S. Luca, C. Idle, A. Chao, Water Sci. Technol. 33 (1996) 119.
[4] L. Delaude, P. Laszlo, J. Org. Chem. 61 (1996) 6360.
[5] R. Audette, J. Quail, P. Smith, J. Chem. Soc., Chem. Commun. (1972) 38.
[6] S. Licht, B. Wang, S. Ghosh, Science 285 (1999) 1039.
[7] S. Licht, B. Wang, S. Ghosh, J. Li, V. Naschitz, Electrochem. Commun. 1 (1999) 522.
[8] S. Licht, B. Wang, G. Xu, J. Li, V. Naschitz, Electrochem. Commun. 1 (1999) 527.
[9] S. Licht, B. Wang, Electrochem. Solid State Lett. 3 (2000) 209.
[10] S. Licht, B. Wang, J. Li, S. Ghosh, R. Tel-Vered, Electrochem. Commun. 2 (2000) 535.
[11] S. Licht, V. Naschitz, S. Ghosh, B. Liu, N. Halperine, L. Halperin, D. Rozen, J. Power Sources 99 (2001) 7.
[12] S. Licht, V. Naschitz, L. Lin, J. Chen, S. Ghosh, B. Liu, J. Power Sources 101 (2001) 167.
[13] S. Licht, V. Naschitz, S. Ghosh, L. Lin, B. Liu, Electrochem. Commun. 3 (2001) 340.
[14] S. Licht, S. Ghosh, V. Naschitz, N. Halperin, L. Halperin, J. Phys. Chem. B 105 (2001) 11933.
[15] S. Licht, S. Ghosh, Q. Dong, J. Electrochem. Soc. 148 (2001) A1072.
[16] S. Licht, V. Naschitz, S. Ghosh, Electrochem. Solid State Lett. 4 (2001) A209.
[17] S. Licht, R. Tel-Vered, L. Halperin, Electrochem. Commun. 4 (2002) 933.
[18] S. Licht, V. Naschitz, B. Wang, J. Power Sources 109 (2002) 67.
[19] S. Licht, S. Ghosh, J. Power Sources 109/2 (2002) 465.
[20] S. Licht, V. Naschitz, S. Ghosh, J. Phys. Chem. B 106 (2002) 5947.
[21] R. Tel-Vered, D. Rozen, S. Licht, J. Electrochem. Soc. 150 (2003) A1671.
[22] S. Ghosh, W. Wen, R.C. Urian, C. Heath, V. Srinivasamurthi, W. Reiff, S. Mukerjee, V. Naschitz, S. Licht, Electrochem. Solid State Lett. 6 (2003) A260.
[23] S. Licht, R. Tel-Vered, L. Halperin, J. Electrochem. Soc. 151 (2004) A31.
[24] S. Licht, R. Tel-Vered, Chem. Commun. (2004) 628.
[25] S. Licht, V. Naschitz, D. Rozen, N. Halperin, J. Electrochem. Soc. 151 (2004) A1147.
[26] S. Licht, L. Yang, B. Wang, Electrochem. Commun. 7 (2005) 931.
[27] S. Licht, X. Yu, Environ. Sci. Technol. 39 (2005) 8071.
[28] I. Nowik, R.H. Herber, M. Koltypin, D. Aurbach, S. Licht, J. Phys. Chem. Solids 66 (2005) 1307.
[29] M. Koltypin, S. Licht, R. Tel-Vered, V. Naschitz, D. Aurbach, J. Power Sources 146 (2005) 723.
[30] S. Licht, C. DeAlwis, J. Phys. Chem. B 110 (2006) 12394.
[31] S. Licht, X. Yu, D. Zheng, Chem. Commun. (2006) 4341.
[32] M. Koltypin, S. Licht, I. Nowik, E. Levi, Y. Gofer, D. Aurbach, J. Electrochem. Soc. 153 (2006) A32.
[33] W. Yang, J. Wang, T. Pan, J. Xu, J. Zhang, C. Cao, Electrochem. Commun. 4 (2002) 710.
[34] K. Bouzek, M. Schmidt, A. Wragg, Electrochem. Commun. 1 (1999) 370.
[35] J. Lee, D. Tryk, A. Fujishima, S. Park, Chem. Commun. (2002) 486.
[36] M. De Koninck, T. Brousse, D. Belanger, Electrochim. Acta 48 (2003) 1425.
[37] K. Bouzek, I. Roušar, H. Bergmann, K. Hertwig, J. Electroanal. Chem. 425 (1997) 125.
[38] A.A. Kamnev, B. Ezhov, Electrochim. Acta 37 (1992) 607.
[39] S. Licht, L. Halperin, M. Kalina, M. Zidman, N. Halperin, Chem. Commun. (2003) 3006.
[40] S.V. Mentus, Electrochim. Acta 50 (2005) 3609.
[41] C.-C. Hu, K.-Y. Liu, Electrochim. Acta 44 (1999) 2727.
[42] S.R. Ovshinsky, M. Fetcenko, J. Ross, Science 260 (1993) 176.
[43] D. Aurbach, M.L. Daroux, P. Faguy, E.J. Yeager, J. Electroanal. Chem. Interfacial Electrochem. 297 (1991) 225.